

We are IntechOpen, the world's leading publisher of Open Access books Built by scientists, for scientists

6,900

Open access books available

186,000

International authors and editors

200M

Downloads

Our authors are among the

154

Countries delivered to

TOP 1%

most cited scientists

12.2%

Contributors from top 500 universities



WEB OF SCIENCE™

Selection of our books indexed in the Book Citation Index
in Web of Science™ Core Collection (BKCI)

Interested in publishing with us?
Contact book.department@intechopen.com

Numbers displayed above are based on latest data collected.
For more information visit www.intechopen.com



Label-Free Biosensing Using Photonic Crystal Waveguides

Jaime García-Rupérez, Veronica Toccafondo and Javier García Castelló
*Nanophotonics Technology Center, Universidad Politécnica de Valencia
Spain*

1. Introduction

The development of fast, efficient, and reliable sensing devices to be used for the detection, identification, and quantification of substances and biological material is one of the main current investigation fields. Among the substances and analytes to be detected we can find gases, liquids, proteins, hormones, bacteria, or DNA. These sensing devices can find applications in many fields, such as medical diagnostics, food safety control, environmental control, or drug detection.

Most of the currently available sensing devices base their detection on labelling the target analytes because of the difficulty to directly detect very small size analytes in a low concentration. By performing a proper treatment of the sample in which the target analyte is contained, it is possible to attach a label to it. The label consists of a material with certain physical properties such as fluorescence, radioactivity, metallic material, etc. so that the analyte detection is indirectly carried out by detecting the physical properties of the label that has been attached to it. However, although analyte labelling is an effective way to detect small size analytes in a small concentration, it requires previous sample preparation which needs to be performed by skilled personnel and is time consuming. Moreover labelling presents the difficulty of finding a proper method to specifically attach the labels only to the target analyte to be detected. It is therefore important to have more sensitive sensing devices or mechanisms at our disposal, which allow performing the detection without the need of labels.

One of the main candidates for the development of these highly sensitive sensing devices able to perform a label-free detection is photonic technology (Fan et al., 2008), and more specifically, integrated planar photonic devices, which have been attracting an increasing interest in the last few years. Although more mature photonic sensing technologies, such as those based on surface plasmon resonances (Homola et al., 1999) or fiber Bragg gratings (Kersey et al., 1997), have even become commercially available some years ago, devices based on integrated planar photonic structures are envisaged as a highly promising alternative for future lab-on-a-chip (LoC) devices.

First demonstrations of the possibility of using these devices for sensing applications were reported by the end of the past century, as for example in (Luff et al., 1996) and (Schubert et al., 1997), but it has not been until 5-6 years ago that many researchers have focused their

investigations on the application of already developed integrated planar photonic devices for biosensing purposes. The transduction principle of these devices is based on the high dependence of their response to changes in the refractive index (RI) of the surrounding medium. Therefore, when the target analyte is deposited on the top (or generally, the surroundings) of the photonic structure, it induces a RI variation which can be directly detected by means of the change in the device's response.

The two main advantages of integrated planar photonic devices for sensing applications are their high sensitivity due to the high confinement of the electromagnetic field in the photonic structure which enhances the interaction with the target analyte, and their reduced size, which makes it possible both to detect very small analytes and to integrate many of these devices on a single chip to perform a multi-analyte detection. Other advantages of integrated photonic sensing devices are derived from these two, such as a short analysis time, the possibility to perform a label-free detection avoiding a costly previous sample preparation procedure (in terms of time and money), or the requirement of very low volumes of analyte and reagents to perform the analysis. Moreover, if these integrated planar photonic devices are based on CMOS-compatible materials such as Silicon-On-Insulator (SOI), the possibility of using mass manufacturing techniques for the fabrication opens the door to a low cost and high volume production of these devices.

Many different integrated planar photonic structures are widely used for sensing applications, among which resonant structures, Mach-Zehnder Interferometers (MZIs), and photonic crystal structures are the most common. Results reported using these structures range from basic characterization of the sensing device to refractive index variations to more complex bio-sensing experiments where the presence of a specific analyte such as proteins, bacteria or even DNA strands is detected and quantified without the need of any label.

The most popular integrated planar photonic sensing devices are probably those based on resonant structures such as rings or disks, which are coupled to an access waveguide (De Vos et al., 2007, 2009; Barrios et al., 2008; Ramachandran et al., 2008; Carlborg et al., 2010; Iqbal et al., 2010; Xu et al., 2010a). In these structures, variations on the surrounding media provoke a spectral shift of the transmission resonances, which is used to perform the sensing. These kind of sensing structures exhibit high sensitivity and low detection limit values, with a small footprint on the order of a few hundreds of μm^2 .

Other groups work on the development of photonic biosensors using Mach-Zehnder Interferometers (MZIs) (Schubert et al., 1997; Sepulveda et al., 2006; Densmore et al., 2009), where changes in the refractive index in the proximity of one of the arms provoke an additional phase shift over the propagated wave which is translated into an amplitude variation at the output. Although these sensing structures exhibit performances similar to or even better than resonant structures, their main problem is that very long arm lengths (of some millimetres) are required in order to provide enough interaction to detect the presence of the analyte, thus limiting their integration level. Nevertheless, this issue has been greatly overcome by folding the arms of the MZI, thus significantly reducing the final footprint of the device (Densmore et al., 2009).

The third main alternative for the development of integrated planar photonic biosensors are photonic crystal structures, on which this chapter will focus. Several configurations are typically used when developing photonic crystal based sensing structures: bulk photonic

crystals (Huang et al., 2009), photonic crystal waveguides (Skivesen et al., 2007; Buswell et al., 2008; Di Falco et al., 2009; García-Rupérez et al., 2010; Toccafondo et al., 2010; Scullion et al., 2011), and photonic crystal cavities (Loncar et al., 2003; Chow et al., 2004; Lee & Fauchet, 2007; Sünner et al., 2008; Dorfner et al., 2009; Zlatanovic et al., 2009; Xu et al., 2010b). For bulk photonic crystal sensors, the periodic dielectric structure does not present any defects and it is directly used to perform the sensing. For these structures, a variation of the refractive index of the surrounding medium provokes a shift of the position of the photonic bandgap (PBG) edge, which is used to perform the sensing. However, when using bulk photonic crystals, light is not well localized on the in-plane direction of the structure, so that configurations where linear or punctual defects are introduced on the bulk structure are usually preferred in order to enhance the localization of the optical field in an active region well below $100 \mu\text{m}^2$ and thus increase the interaction with the target analyte.

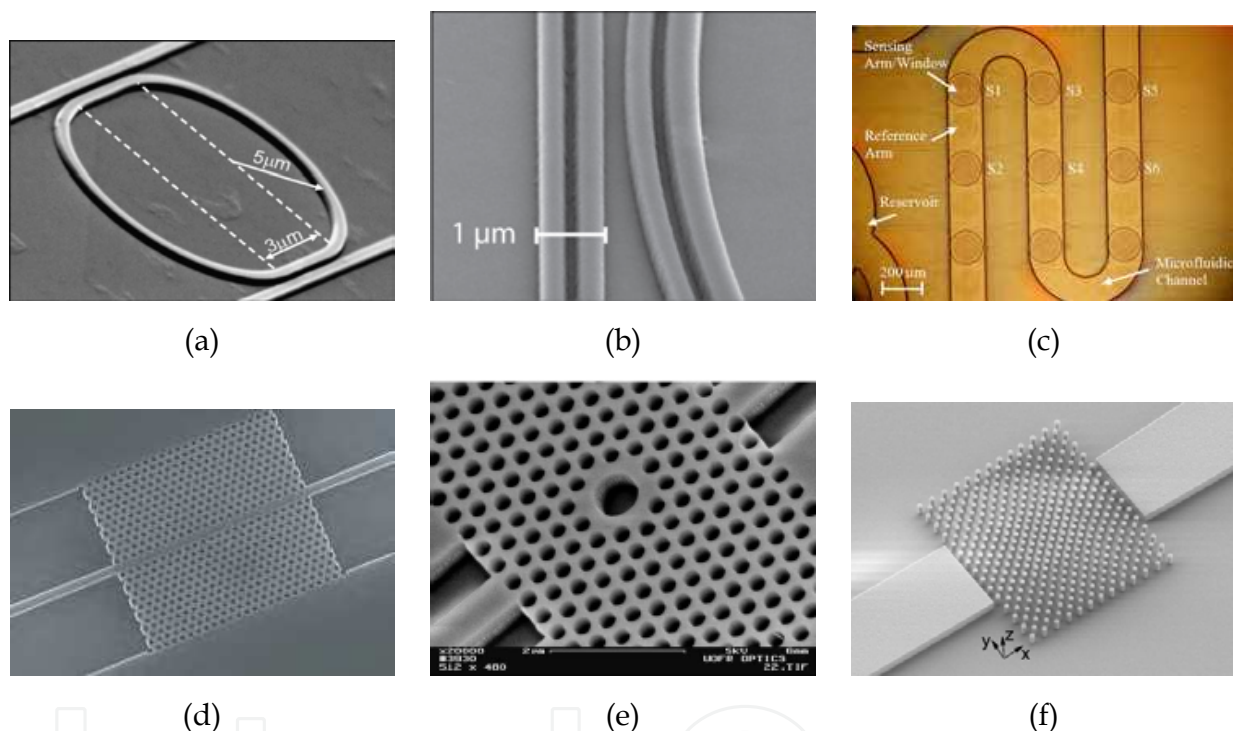


Fig. 1. SEM (Scanning Electron Microscope) pictures of several integrated planar photonic structures for sensing purposes. (a) SOI ring resonator (De Vos et al., 2007); (b) coupling region of a silicon nitride slot ring resonator (Carlborg et al., 2010); (c) array of SOI MZIs with folded arms (Densmore et al., 2009); (d) SOI photonic crystal waveguide (Buswell et al., 2008); (e) holes-based SOI photonic crystal cavity (Lee & Fauchet, 2007); (f) pillar based silicon photonic crystal cavity (Xu et al., 2010b).

For photonic crystal waveguide (PCW) based sensors, a linear defect is introduced in the propagation direction of the optical wave. In this way, light is localized in the region of the linear defect (and its surroundings), leading to an increased interaction with the target analyte. When the linear defect is created within the bulk photonic crystal, a guided mode appears inside the PBG of the photonic crystal structure. The position of the guided band edge (either lower band edge or upper band edge) is used for sensing, as it is dependent on the refractive index variations of the surrounding media.

For photonic crystal cavity based sensors, a punctual or area defect is created in the bulk photonic crystal, leading to the formation of a resonator with a strong localization of the optical field within this region. This can be achieved for instance by changing the dimensions of one or several elements of the periodic structure (see Figs. 1.(e) and 1.(f)), or by eliminating them. The coupling of light to this defect is usually achieved in two different manners:

- The defect is created in the bulk photonic crystal, and light is directly coupled to/from it through the access dielectric waveguides. In this configuration, a resonant mode appears inside the PBG of the photonic crystal structure, with a central wavelength determined by the defect profile.
- The defect is created next to the linear defect of a photonic crystal waveguide. In this configuration, light matching the resonance wavelength of the cavity is extracted from the PCW, leading to the appearance of a notch-like response in the transmission spectrum.

For both cases, the resonance position depends on the refractive index of the medium surrounding the cavity region, leading to a very high sensitivity to variations produced in a very small active region, which can even be smaller than $1 \mu\text{m}^2$.

Finally, it is also worth noting that planar 1D periodic waveguides or cavities, such as the ones shown in Fig. 2, which are not usually referred to as photonic crystal structures although they are based in the same principles as them, are also a very promising alternative for the development of integrated planar photonic biosensors (García et al., 2008; Kauppinen et al., 2009; Goddard et al., 2010; Castelló et al., 2011). When using a planar 1D periodic structure, the position of its guided bands or resonant modes is also highly dependant on the refractive index of the surrounding media, so shifts in their position can be used to perform the sensing. Moreover, these structures can be simpler to fabricate and have a smaller footprint than 2D photonic crystal based structures.



Fig. 2. SEM pictures of two planar 1D periodic structures used for sensing purposes. (a) 1D SOI holes cavity (Goddard et al., 2010); (b) 1D SOI corrugated waveguide (Castelló et al., 2011).

The next sections of this chapter will focus on the use of photonic crystal waveguides for the development of label-free photonic biosensors, as they are very promising thanks to their high sensitivity and small footprint. However, the performance of these sensors may be limited by the difficulty to accurately determine the position of the edge of the guided band

of the PCW as this feature is not sharp enough to provide very low uncertainty. This problem can be overcome by using the sharp Fabry-Perot fringes appearing in the slow-light regime near the edge of the guided band, whose position can be determined very accurately, as will be explained in section 2. Moreover, their use ensures that we are working in the slow-light regime of the PCW, which allows a stronger interaction of the optical field with the target substance. In sections 3, 4 and 5, the application of PCW-based biosensors for the detection of refractive index variations, label-free antibody detection, and label-free DNA detection will be shown. Finally, section 6 will describe an alternative method for the indirect measurement of the shift of the guided band's edge, which will allow having a low-cost and real-time sensing system.

2. Photonic crystal waveguide sensor design and sensing principle

Planar PCWs are one of the preferred photonic structures for the development of biosensing devices because of their reduced size and the high confinement of the optical field in the linear defect region. In this text, we will consider planar SOI PCWs, due to the compatibility of this technological platform with CMOS fabrication techniques.

When designing a PCW for biosensing there are several factors to be taken into account. We will focus on five of them:

- First, we have to select between a pillars-on-air or a holes-on-dielectric photonic crystal structure. For pillars-on-air photonic crystals (Xu et al., 2010b), we can have a higher interaction with the target analyte flowing through the pillars; however, light coupling to these structures is less efficient, and their fabrication process can be more complex. On the other hand, for holes-on-dielectric photonic crystals (Buswell et al., 2008), the fabrication process is easier and the light coupling is more efficient, but a weaker interaction with the target analyte is produced. The photonic crystal configuration will also determine the working polarization, as pillars-on-air photonic crystals present PBGs for TM-polarization and holes-on-dielectric photonic crystals present PBGs for TE-polarization.
- We have to select the working wavelength, which is usually determined by the available readout system and light sources, so that typically used wavelengths are those from telecom applications: around 1310 nm and around 1550 nm. A working wavelength around 1310 nm allows having lower water absorption losses, however this is not really a critical point because power is not a major issue for integrated photonic biosensors. On the other hand, working at higher wavelengths, such as 1550 nm, makes the evanescent field wider and thus provides a higher sensitivity.
- The thickness of the patterned silicon layer will also affect the sensitivity of the device; the thinner the silicon layer, the higher the sensitivity because of the larger amount of evanescent field traveling through the upper cladding and interacting with the target analytes. This parameter is usually set by the SOI substrates used to fabricate the devices.
- The PCW configuration will also affect the sensitivity of the sensing device. Again, the configuration with a higher amount of evanescent field traveling through the cladding will provide a higher sensitivity due to an enhanced interaction between the optical field and the target analyte.

- Finally, the interface between the PCW and the access waveguide is also something to be taken into account. As previously commented, the shift of the guided band's edge is used in PCW to perform the sensing. Therefore, it is important to have a PCW with a sharp band edge in order to be able to accurately determine its position.

PCWs are designed by means of simulations to determine their optimal parameters and match the previously commented criteria. The most widely used simulation techniques for the design of photonic crystals are FDTD (Finite-Differences Time-Domain), which is used to calculate the propagation of the electromagnetic wave through the structure, and the plane-wave expansion (PWE) method, which is used to determine the band diagram of the perfect infinite photonic crystal structure.

Now the design and experimental characterization of a PCW sample for biosensing will be described. We will consider a PCW in a holes-on-dielectric photonic crystal fabricated on a SOI wafer with a 250nm-thick silicon layer on a 3 μ m-thick buried oxide layer. The PCW will be a W1-type, where one row of holes is removed in the Γ -K direction to create the waveguide. The PCW was designed to have a working wavelength located around $\lambda = 1550$ nm.

By PWE simulations, the lattice constant and the hole radius which will yield a guided band's edge located around 1550 nm can be determined. In case we decide to have the upper edge (in terms of wavelength) of the guided band around this wavelength, these parameters must be 390 nm and 110 nm, respectively. Fig. 3 shows the band diagram for TE-modes calculated for the holes-on-silicon W1-PCW using the PWE method, where the fundamental mode of the PCW with its upper edge located around 1550 nm can be seen.

The next step is the fabrication of the PCW on a SOI substrate. For the fabrication of holes-on-dielectric photonic crystal structures, the lithographic process is usually carried out using a positive resist such as PMMA, where the holes area and the trenches defining the structure need to be exposed by e-beam or DUV lithography. After developing the resist, the pattern is transferred to the silicon layer by an etching process such as inductively coupled plasma (ICP) etching.

Fig. 4 shows a scanning electron microscopy (SEM) picture of a W1-PCW fabricated to be used for biosensing. The structural parameters of this PCW were determined by the theoretical simulations, and its length is 20 μ m (\approx 52 periods), which provide enough periods for achieving a strong photonic bandgap effect while keeping the structure size as compact as possible. For coupling, 450nm-wide single-mode access waveguides are used to couple/collect light to/from the PCW. The interface between the PCW and the single-mode access waveguides is the one shown in Fig. 4, where the structure ends next to the inner row of holes of the PCW. This interface presents a sharper band edge than other interfaces.

For the optical characterization of the PCW, which is essentially determined by its transmission spectrum, light from an external source must be coupled to the chip. The two main coupling mechanisms used for chip's characterization are butt coupling, where light from a lensed fiber is laterally coupled to the chip, and grating couplers, where light is vertically coupled to the chip using grating structures. For the characterization of these PCW sensors, light from a tunable laser is TE-polarized using a polarization controller and butt-coupled into the PCW using a lensed fiber. Output light is then collected using an objective

and detected using an optical powermeter after passing through a free-space polarizer configured for TE polarization. Since the fabricated PCWs are designed for biosensing applications, and these require the use of the sensors in a wet environment, the design was optimized for these working conditions. Fig. 5 thus shows the transmission spectrum of one of the fabricated PCWs when deionized water (DIW, $n = 1.3173$) is used as upper cladding. Sharp peaks can be observed at the edge of the guided band (located around 1563 nm).

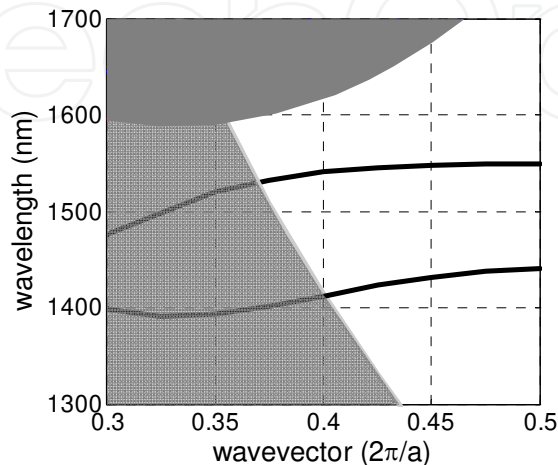


Fig. 3. Band diagram for TE modes of the SOI W1-PCW with a silicon thickness of 250 nm, a hole radius of 110 nm and a lattice constant of 390 nm. Dark and light shaded areas depict modes going into the bulk photonic crystal and the silicon oxide lower cladding, respectively.

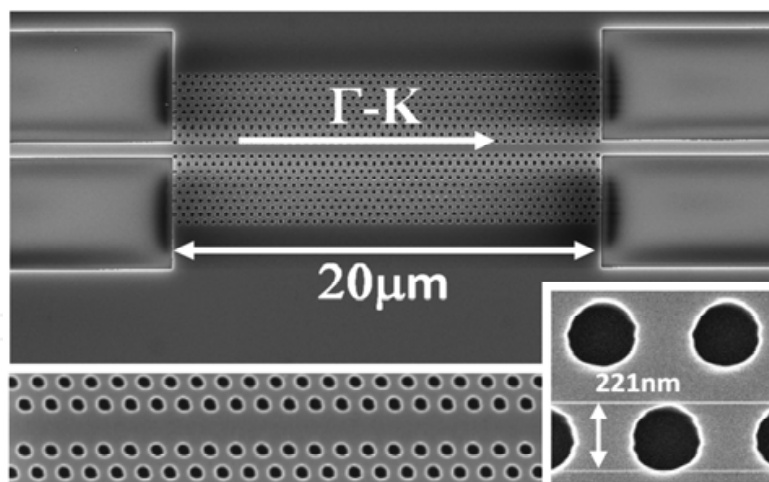


Fig. 4. SEM image of the SOI photonic crystal waveguide used for the sensing, with close-up view of the sensor area and photonic crystal holes (insets)

Fringes appearing near the band edge of the transmission spectrum of the PCW are Fabry-Perot (FP) fringes of the cavity defined by the interface between the PCW and the access waveguides (García et al., 2006), as schematically depicted in Fig. 6. A good power coupling between modes in the access waveguides and the PCW is achieved for wavelengths in the transmission band, making the FP cavity effect almost negligible. However, mode mismatching increases between the two waveguides as we get closer to the edge of the

guided band, thus reducing the coupling efficiency and increasing the reflected power, so higher amplitude FP fringes begin to appear. Not only is there an increase of the reflection coefficient at the interfaces (and thus a reduction of the transmission coefficient), but also a reduction of the group velocity of the guided mode of the PCW as we get closer to the edge of the Brillouin zone. The reduction of the group velocity makes the optical length of the FP cavity longer, thus increasing the frequency of the FP fringes of the transmission spectrum in the region of the band edge. The main point of using these fringes to perform the biosensing is that we are working in the slow-light regime of the PCW, so we will have a higher interaction of the electromagnetic field with the target analyte.

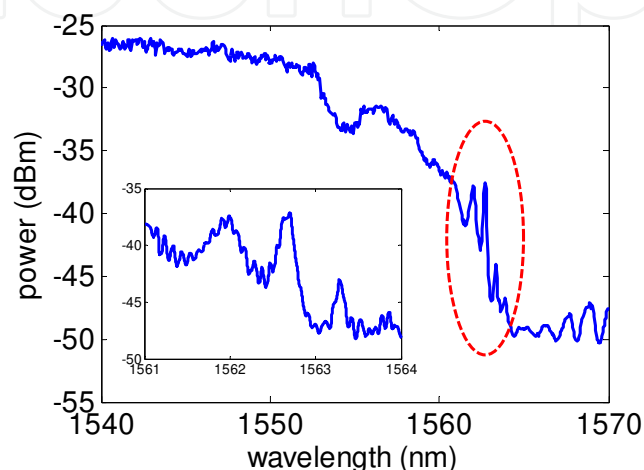


Fig. 5. Spectrum of the PCW in the region of the band edge when having DIW as upper cladding. Transmission fringes at the band edge are marked with dashed red line and enlarged in the inset.

From expressions shown in Fig. 6.(b), it can be seen that the transmission spectrum is dependent on both the transmission and reflection coefficients at the interfaces and the propagation constant of the guided mode in the PCW, which determines the optical length of the structure. Fig. 7.(a) shows these three parameters (transmission and reflection coefficients between the access waveguides and the PCW, and propagation constant of the PCW guided mode) obtained using the numerical tool CAMFR, which is based in the eigenmode expansion (EME) method, for the PCW with interface with the access waveguides as shown in Fig. 6.(a). Note that only the reflection coefficient for the incidence from the PCW to the access waveguide (r_{21} , r_{23}) is needed for the calculations and that the transmission coefficient is the same for the incidence from the PCW to the access waveguide and vice versa due to reciprocity properties ($t_{ij} = t_{ji}$). Although this software does not allow 3D calculations, a generic 2D modelling (i.e., infinite height of the structure) using an effective refractive index of 2.8 for the silicon slab and 1.33 for the cladding surrounding the structure is useful to realistically predict the appearance of FP fringes in the transmission spectrum. It can be seen that the transmission coefficient decreases to zero as we get closer to the band edge (the opposite is true for the reflection coefficient, which tends to one), thus the amount of power coupled into the PCW decreases and a stronger cavity effect is created. Concerning the propagation constant, it can be seen that it gets flatter as the edge of the guided band is approached, which means a reduction on the group velocity (which tends to zero) and makes the fringes narrower

and closer between them. This reduction in the group velocity will also provoke a higher interaction of the optical field with the target analytes.

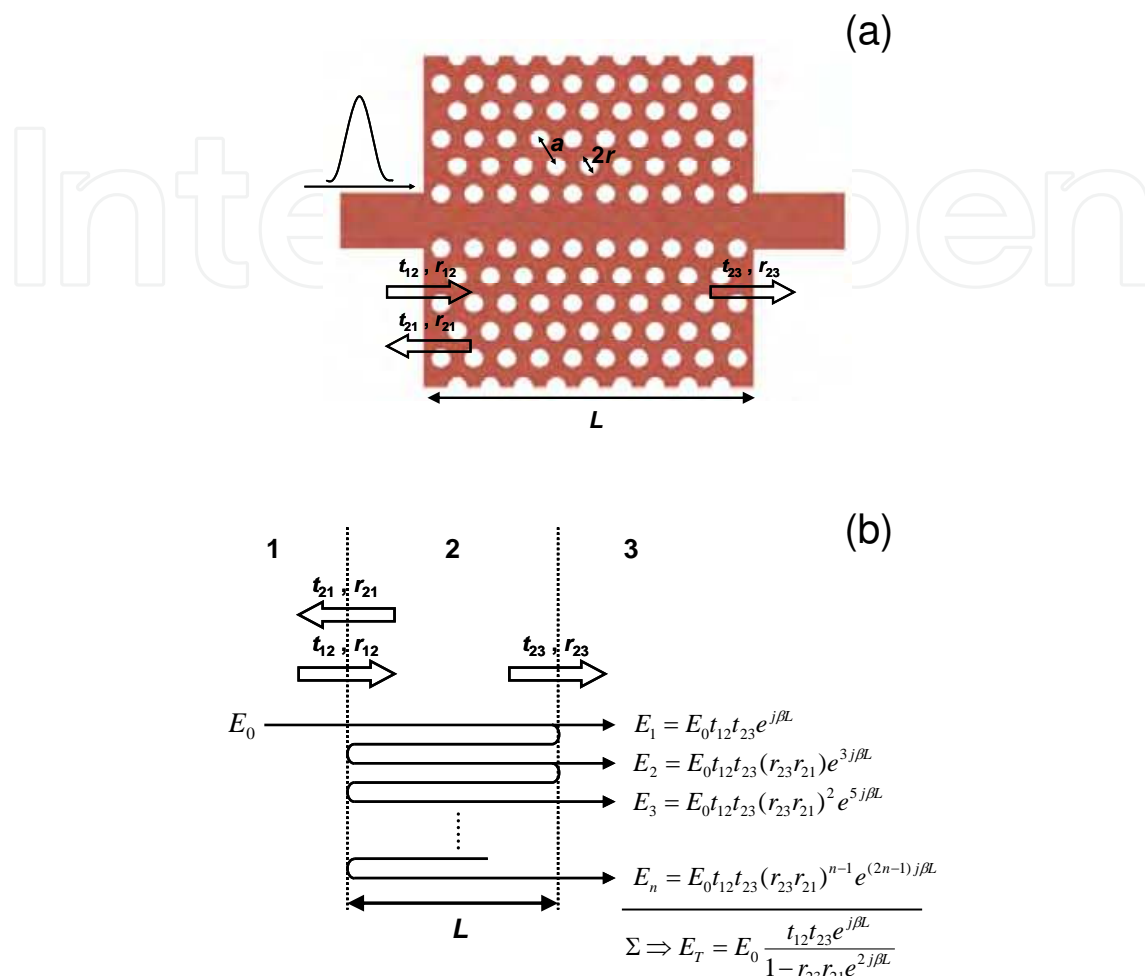


Fig. 6. (a) Schematic picture of the PCW with its access waveguides. The interface with the access waveguides is that of the fabricated PCW. The structural parameters of the PCW (i.e., lattice constant, hole radius and PCW length), and the transmission and reflection coefficients at each interface (t_{ij} , r_{ij}) are depicted. (b) All signal contributions generated in the PCW because of the reflections at the interfaces with the access waveguides are combined at the output, being responsible of the appearance of FP oscillations in the transmission spectrum. Media 1 and 3 represent the access waveguides and medium 2 represents the PCW.

When these three parameters are combined using the expression shown in Fig. 6.(b), the transmission response shown in Fig. 7.(b) for a 20 μm -long 2D-PCW is obtained. One can see how FP resonances appear because of the cavity created inside the PCW, and how these FP fringes get stronger and narrower as we approach the edge of the guided mode because of the increase of the reflection coefficient and the decrease of the group velocity.

To corroborate the appearance of these FP fringes in the edge of the guided mode of the PCW and analyze the potential for using them for biosensing purposes, 3D-FDTD simulations of the PCW with the parameters of the fabricated structure and two different

upper claddings ($n_1 = 1.3173$ and $n_2 = 1.3200$; corresponding to the refractive indices of DIW and a ethanol-DIW 4% dilution) can be performed (in this case, RSoft's FullWAVE software was used). Simulation results for each upper cladding are shown in Fig. 8, where the FP fringes at the band edge are observed again and where the position of the guided band is dependent of the refractive index of the upper cladding. Table 1 shows the wavelength shift and the calculated sensitivity in terms of refractive index units (RIU) for each fringe near the band edge. As predicted from the previous theoretical modeling, an increase in the sensitivity is obtained as we get closer to the guided band edge because of the reduction in the group velocity of the guided mode, obtaining a sensitivity $\sim 40\%$ higher for the fringe closest to the band edge compared to the first of the selected fringes (78.70 nm/RIU vs. 57.15 nm/RIU).

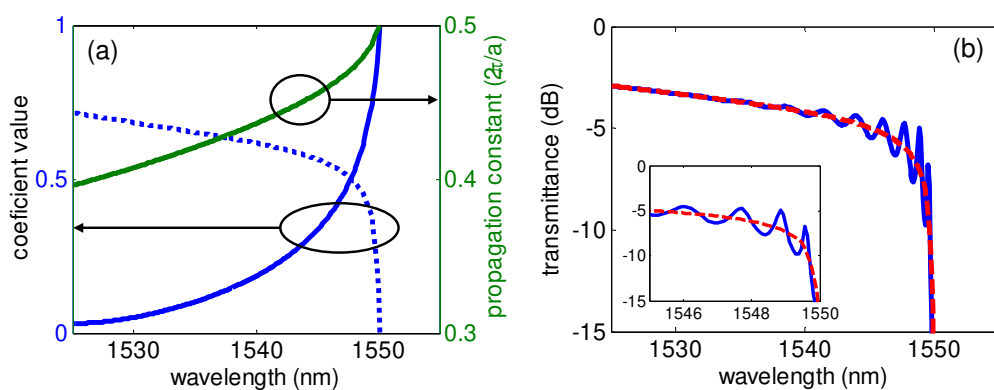


Fig. 7. (a) Theoretical transmission (blue dotted line) and reflection coefficients (blue solid line), and propagation constant of the PCW (green solid line) calculated with CAMFR. (b) Transmission response of the 20 μm -long PCW when the created FP cavity is considered (blue solid line). The transmission response when no cavity is considered (only the direct contribution propagating into the PCW) is also depicted (red dashed line). The inset shows a detail of the transmission band edge.

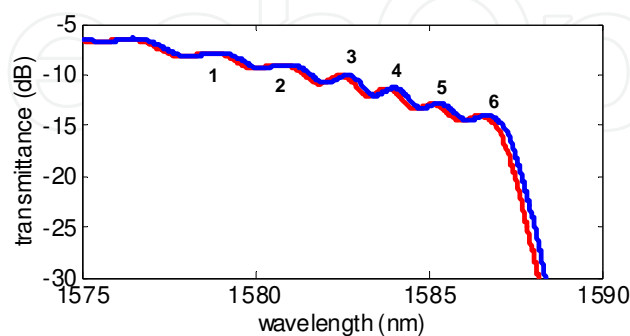


Fig. 8. 3D-FDTD simulations of the transmission spectrum of the 20 μm -long PCW for two different upper claddings: $n_1 = 1.3173$ (red line) and $n_2 = 1.3200$ (blue line). FP fringes near the band edge have been labeled from 1 to 6. The band edge fringes are slightly smoothed because of the stop time used to make the duration of the simulation reasonable.

Fringe #	1	2	3	4	5	6
Wavelength shift (nm)	0.1543	0.1865	0.192	0.2002	0.2039	0.2125
Sensitivity (nm/RIU)	57.15	69.07	71.11	74.15	75.52	78.70

Table 1. Wavelength shift and sensitivity for each FP fringe near the guided band edge for the 3D-FDTD simulations.

3. Refractive index sensing using photonic crystal waveguides

A straight-forward way to test the possibility of using these band edge fringes to perform biosensing, is to carry out a simple refractive index sensing experiment, for instance using several dilutions of ethanol in DIW. Dilution concentrations are (in mass %): pure DIW, ethanol 2% in DIW, and ethanol 4% in DIW, whose refractive indices at $\lambda \approx 1550$ nm and $T = 25^\circ\text{C}$ are 1.3173, 1.3186, and 1.3200, respectively (García-Rupérez et al., 2010).

For carrying out the RI sensing experiments, a flow cell is required in order to flow the target substances over the chip. In this case, a 2-port flow cell with a fluidic cavity of size 5.5mm x 2mm x 0.5mm (length x width x depth) is placed on the top of the chip. For pumping the liquid passing through the flow cell, an automatic syringe pump in withdrawal mode connected to one of the ports of the flow cell using silicone tubing is used. The liquid is flowed at a rate of 15 $\mu\text{l}/\text{min}$. Tubing from the second port of the flow cell is placed into a vial with the liquid to be flowed over the chip. This configuration is used in order to avoid having to replace the syringe to change the liquid to be flowed: with this configuration, the liquid is drawn from vials, enabling an easier handling of the tubes when manual changing between them is performed. The TE transmission spectrum of the PCW in the vicinity of the guided band edge (shown in Fig. 5) is continuously acquired using a tunable laser with a sweep resolution of 10 pm, and a cubic interpolation is used to increase the wavelength accuracy on the determination of the position of the peak's maximum. Fig. 9 shows the temporal evolution of the position of the maximum of the FP peak located around 1563.3 nm for the different ethanol-DIW dilutions flowed.

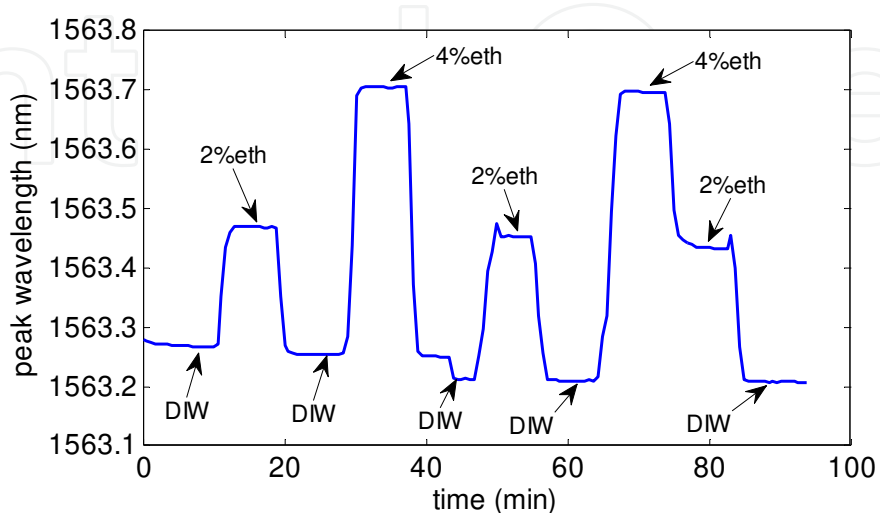


Fig. 9. Temporal evolution of the FP peak for the different ethanol-DIW dilutions flowed.

Fig. 10 shows the relative peak shift for the three ethanol-DIW concentrations used in the experiments, where a linear behavior is observed, with a sensitivity of 118 pm/% calculated with respect to the ethanol concentration. Considering the almost linear RI variation for this ethanol concentration range ($\Delta n \approx 6.75 \times 10^{-4} / \%$), a sensitivity to RI variations of $S = \Delta \lambda / \Delta n = 174.8 \text{ nm/RIU}$ is obtained. This value is 2.2x the value obtained in 3D-FDTD simulations, and this difference can be attributed to the discretization step of the PCW used for the FDTD simulations, which may have led to a non accurate modelling of the optical field which senses the variation of the refractive index of the cladding. The reason for this high sensitivity value is also the higher interaction with the target analyte due to the reduction of the group velocity in the band edge, where the FP fringes used to sense are located.

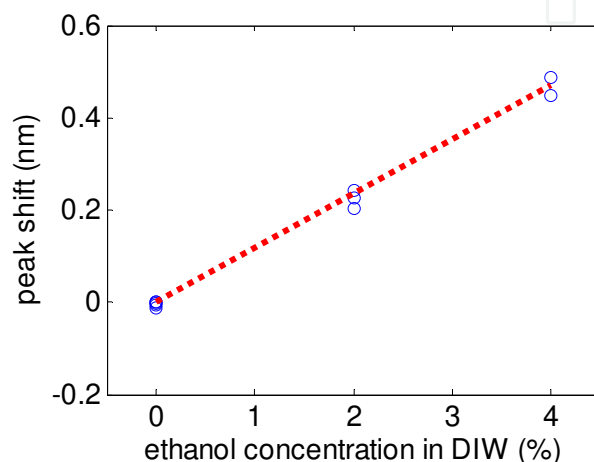


Fig. 10. Blue circles depict the wavelength shift of the position of the maximum of the peak for the different ethanol-DIW dilutions. The linear fit of the data is depicted with dashed red line.

We can then use the standard deviation σ of the peak position for a continuous flow of an ethanol-DIW dilution, which is 0.6 pm, as the noise level, and use it to calculate the theoretical detection limit DL, which is defined as $DL = \sigma / S$. A value as low as $DL = 3.5 \times 10^{-6}$ RIU is obtained.

4. Antibody sensing using photonic crystal waveguides

Once the origin of band edges fringes is modeled and the possibility of using them for sensing purposes is checked by performing RI sensing experiments, they are used for label-free antibody sensing. A different PCW sample (with the same nominal parameters) from another fabrication run is used for this. In order to give specificity to the antibody sensing, the PCW sensing device needs to be bio-functionalized with proper antigen probes which will act as receptors for the target analyte. In this case, anti-BSA (bovine serum albumin) antibody is used for the sensing experiments, so BSA antigen probes need to be immobilized on the surface of the photonic sensor. This bio-functionalization process consists in the activation of the surface of the chip with pure ICPTS (3-isocyanatepropyl triethoxysilane) vapour, the deposition and incubation of BSA antigen 10 $\mu\text{g/ml}$ in PBS 0.1x, and a final blocking step with ovalbumin protein (OVA) 1% in PBS 0.1x (García-Rupérez et al., 2010). The flow cell and the tubing used for the experiments are also blocked with OVA to avoid the absorption of the flowed molecules.

The transmission spectrum for the TE polarization is obtained for the bio-functionalized PCW when having PBS 0.1x as upper cladding, and is shown in Fig. 11, where the band edge is now located around 1542 nm. A closer look at the spectral area close to the band edge is given in Fig. 11.(b), where sharp peaks appearing in this region are once again observed.

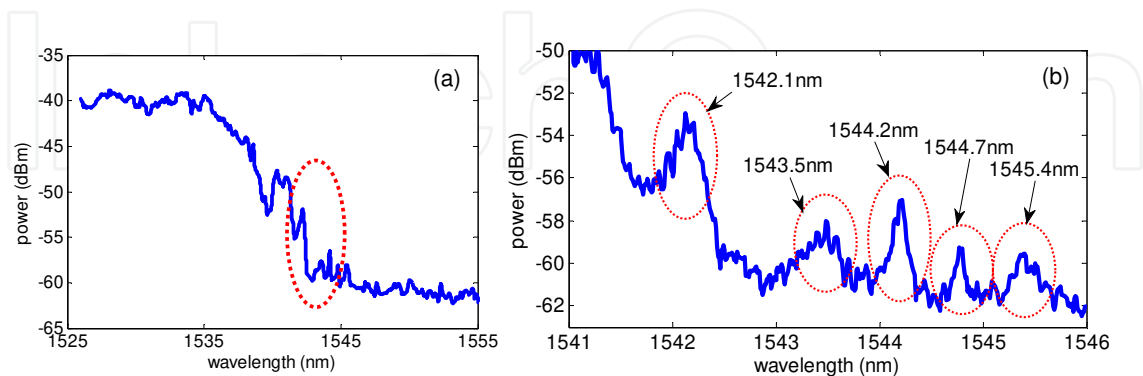


Fig. 11. (a) Spectrum of the PCW in the region of the band edge when PBS 0.1x is flowed. (b) More detailed view of the transmission spectrum close to the band edge. Transmission peaks in this region are marked with dashed red circles and their approximated wavelength positions are depicted.

Fig. 12 shows the temporal evolution of the peak shift for the first four peaks depicted in Fig. 11.(b) (peaks at 1542.1nm, 1543.5nm, 1544.2nm and 1544.7nm) during the whole experiment. The initial baseline is obtained by continuously flowing the PBS 0.1x buffer. Once a stable baseline is achieved, anti-BSA antibody at a concentration of 10 $\mu\text{g}/\text{ml}$ in PBS 0.1x solution is flowed over the chip, which will bind to the BSA probes attached to the PCW surface thus inducing a shift in the peak position. The anti-BSA is flowed long enough to achieve a monolayer on the top of the BSA-functionalized chip, as indicated by the saturation in the shift of the PCW response. Then, the flow is switched back to the PBS 0.1x buffer to remove any anti-BSA which has not specifically bound to probes on the surface of the PCW, thus only the net shift due to the binding of the anti-BSA to the BSA probes is obtained. Finally, a control step is done by flowing an anti-digoxigenin (anti-DIG) antibody 15 $\mu\text{g}/\text{ml}$ in PBS 0.1x dilution to check that the shift previously obtained for the anti-BSA antibody flow is only due to a specific binding to the BSA probes and not due to absorption or any other mechanism. Because of the low affinity between the anti-DIG and the BSA probes, a very slight peak shift is observed during this flow. Later, PBS 0.1x is flowed again to finish the experiment.

One can see from Fig. 12 that the temporal evolution is almost the same for all the tracked peaks, reaching a plateau for the anti-BSA flow, indicating the formation of a monolayer. Concerning the total shift when the anti-BSA is flowed, it is slightly different for each peak, as shown in Table 2. The shift is higher as we move to peaks closer to the band edge (i.e., from peak #1 to peak #4). This is due to the reduction of the group velocity of the guided mode and was already observed in the 3D-FDTD simulations for RI sensing. However, peak #3 does not follow this trend and shows a wavelength shift smaller than peak #2 (this fact will be commented later).

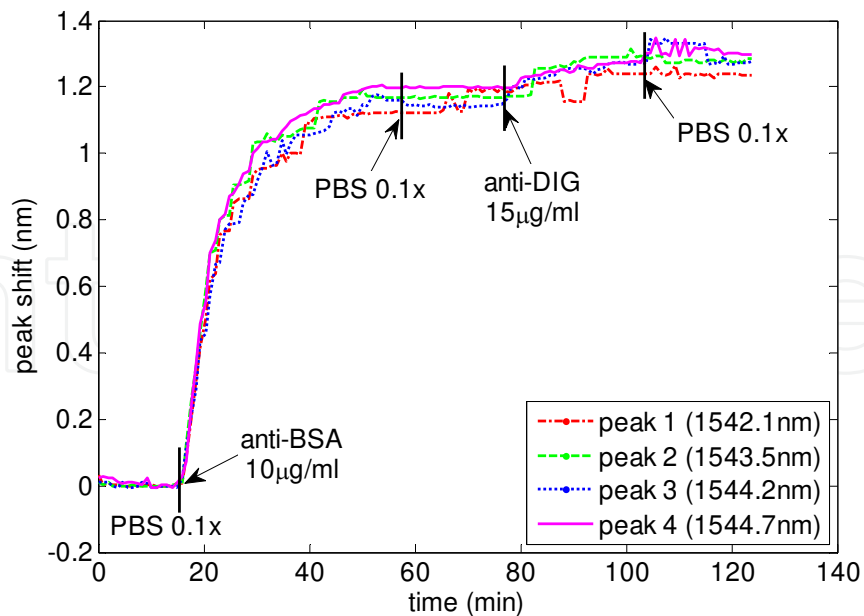


Fig. 12. Wavelength shift vs time for the different solutions flowed in the experiment. Each line (color and style identified in the legend) correspond to the relative shift of each tracked peak respect its initial wavelength position. The time instants when the flowed solution is switched are depicted in the figure.

The surface density for a close-packed anti-BSA monolayer when considering a 100% binding efficiency is $\rho_{\text{anti-BSA}} = 1.7 \text{ ng/mm}^2$, which is calculated from the molecular mass and the size of the anti-BSA molecule (as described in (Barrios et al., 2008)), and will give us an upper limit for the detection limit of the device (in the real situation there is no close-pack monolayer as binding efficiency is below 100%). The sensitivity for the anti-BSA detection is given by $S_{\text{anti-BSA}} = \Delta\lambda_{\text{anti-BSA}}/\rho_{\text{anti-BSA}}$; calculated values for each peak are shown in Table 2.

Peak	λ_{initial} (nm)	$\Delta\lambda_{\text{anti-BSA}}$ (nm)	$S_{\text{anti-BSA}}$ (nm/ng/mm ²)	σ_{PBS} (pm)	$DL_{\text{anti-BSA}}$ (pg/mm ²)	$DL_{\text{anti-BSA}}$ (fg)	$\Delta\lambda_{\text{anti-DIG}}$ (nm)
#1	1542.128	1.123	0.661	1.5	2.3	0.23	0.114
#2	1543.471	1.17	0.688	1.5	2.2	0.22	0.108
#3	1544.235	1.142	0.672	3.1	4.6	0.46	0.128
#4	1544.75	1.2	0.706	1.5	2.1	0.21	0.1

Table 2. Parameters characterizing the performance of the FP resonances used for the sensing experiments.

The noise level values obtained in the tracking of each peak, which correspond to the standard deviation of the peak position (σ) for the stable PBS 0.1x cycle flowed after the anti-BSA, are shown in Table 2. It can be seen that the noise level is very low ($\sigma = 1.5 \text{ pm}$), except for peak #3, for which the noise level is twice this value ($\sigma = 3.1 \text{ pm}$). With these noise values and the sensitivities previously calculated for each peak, the surface mass density detection limits (given by $DL_{\text{anti-BSA}} = \sigma_{\text{PBS}}/S_{\text{anti-BSA}}$) are calculated, which are shown in Table 2 for each

peak. A surface mass density detection limit of $<2.1 \text{ pg/mm}^2$ is obtained from the calculations.

The total mass detection limit can also be obtained from the surface mass density detection limit. If the active region of the PCW is considered for the calculations, since it is where the optical field is confined and where the interaction with the target anti-BSA is actually taking place (around two-three rows of holes at each side of the linear defect, which is around $100 \text{ }\mu\text{m}^2$ considering the internal surface of the holes too), a total mass detection limit of $\sim 0.2 \text{ fg}$ is obtained.

Concerning the improvement because of the reduction of the group velocity, Table 2 shows how calculated values for the sensitivity and the detection limit slightly improve as we move closer to the band edge (peak #3 is the only which does not follow this trend and also has a higher noise level, suggesting that it has a poorer quality than the other peaks used in the experiments), although only a 10% improvement is obtained when moving from peak #1 to #4. This is the same increase that was predicted by the 3D-FDTD simulations when taking into account only the four peaks closest to the band edge.

The high sensitivity values which are achieved when working in the wavelength region close to the band edge of the PCW, together with the device's small footprint, make it suitable for the detection of very small amounts of analyte.

5. DNA sensing using photonic crystal waveguides

For label-free DNA sensing, the experimental protocol is similar to the one previously described for antibody sensing, but now the goal of the experiment is to detect DNA hybridization events occurring on the sensor surface, so single DNA strands (ssDNA) need to be immobilized on the PCW. To do so, the chip's surface is still activated with pure ICPTS as described for the antiBSA sensing in the previous section, then an intermediate layer of streptavidin is deposited on the chip (a concentration of 0.1 mg/ml in 0.1x PBS is used), and finally biotinylated ssDNA probes $10 \text{ }\mu\text{M}$ in PBS 0.1x are incubated on the sample, which will bind to the streptavidin layer thanks to the high affinity between the streptavidin and the biotin molecules (Toccafondo et al., 2010). Fig. 13 shows the TE transmission spectrum of the PCW with a PBS 0.1x upper cladding, where FP fringes are shown. In this case, the peak marked with dashed red line has been used for sensing. Fig. 14 shows the steps to be carried out in the experiment and Fig. 15 shows the temporal evolution of the peak position for the different solutions flowed. First of all PBS 0.1x is flowed to obtain the baseline of the measurement. Then a solution containing the complementary ssDNA to that immobilized on the chip, with a concentration of $0.5 \text{ }\mu\text{M}$, is flowed. Binding of the complementary DNA is effectively shown, which induces a shift in the peak position of $\Delta\lambda_{\text{DNA}} = 47.1 \text{ pm}$. The noise level in this experiment is estimated to be $\sigma = 1.865 \text{ pm}$, thus giving an estimated detection limit of 19.8nM for ssDNA hybridization detection.

The strand-end of the complementary ssDNA chosen for this experiment is marked with digoxigenin, in order to allow to perform a control step and confirm the hybridization events. Therefore, after the complementary ssDNA is detected, anti-DIG 10ppm , which has a high affinity with DIG, is flowed. Its binding to the DIG marker of the target ssDNA causes a permanent shift in the peak position of 0.246 nm , which confirms the specific binding of the target DIG-marked ssDNA on the chip.

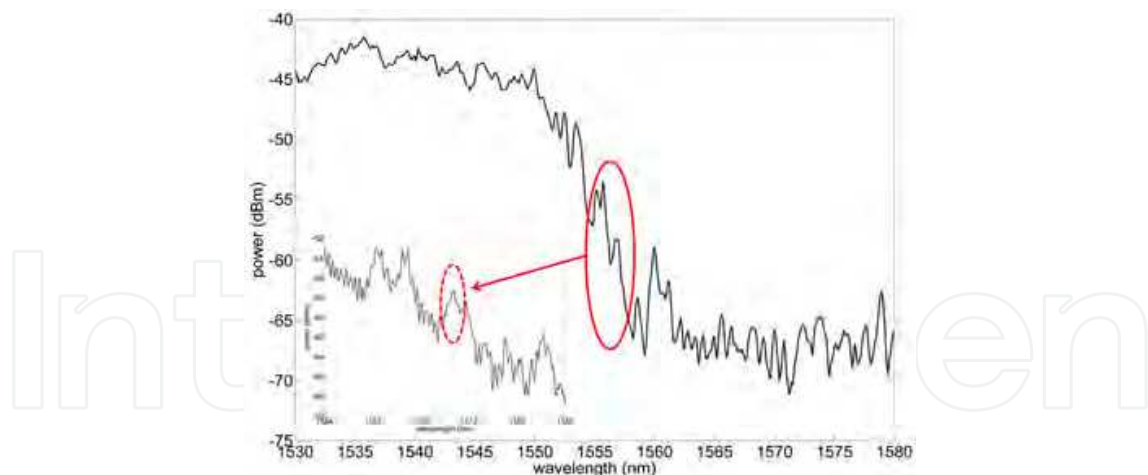


Fig. 13. Spectrum of the photonic crystal waveguide in the region of the band edge with a PBS 0.1x upper cladding. The transmission peak used for sensing is marked with dashed red line in the inset, where a higher resolution sweep has been made.

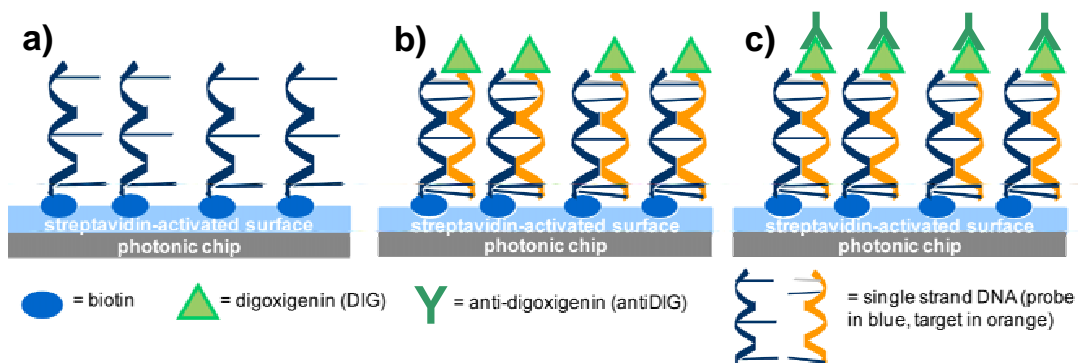


Fig. 14. Scheme of the experiment steps for the ssDNA detection and anti-DIG control.

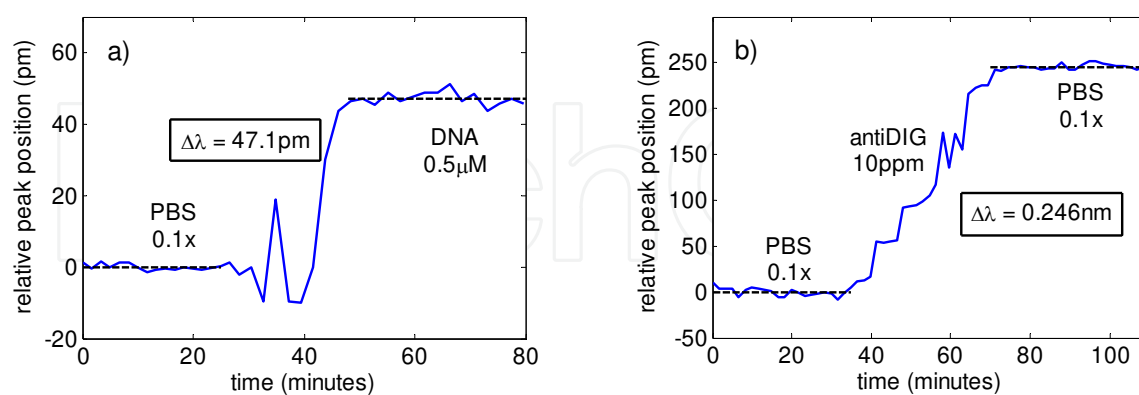


Fig. 15. (a) Wavelength shift vs time for single strand DNA 0.5 μM sensing, and (b) for anti-DIG 10 ppm sensing. Relative wavelength shift from the initial baseline is represented.

6. Low-cost sensing technique using photonic crystal waveguides

One of the problems of using PCWs for biosensing, as well as of other photonic structures like ring resonators, is that the detection is based on the measurement of the shift of the

structure's spectral response, as previously discussed in this chapter. Therefore, these systems require the use of either a tunable laser source or an optical spectrum analyzer (OSA) to perform the readout of the device, making the total cost of the system significant (above 20.000-30.000 Euros or even higher). Moreover, sweeping times of the order of several seconds up to minutes are needed to acquire each spectrum, preventing an instantaneous observation of the interactions of the target analyte with the sensor.

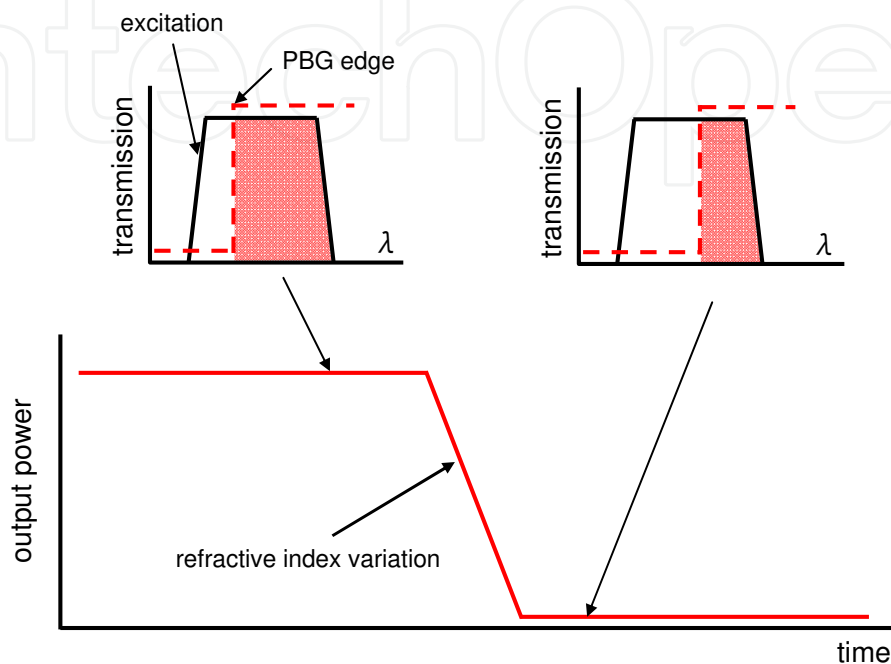


Fig. 16. Output power evolution using the proposed sensing technique. In the initial state, the source spectrum (black solid line) is filtered by the PBG of the sensing structure (red dashed line) and only a certain amount of power is transmitted (shaded area). When a refractive index variation occurs, the PBG shifts, and the amount of input power filtered changes (decreases in this case).

An alternative technique for the development of real-time and low-cost integrated photonic sensing devices using photonic bandgap (PBG) structures is schematically described in Fig. 16. Using this technique, the PBG shift is indirectly determined by using a filtered broadband optical source as excitation instead of a tunable laser, and a power meter at the output instead of an eventual OSA, thus significantly simplifying the system and reducing its cost to values around 2.000-3.000 Euros (or even lower), making it competitive with other sensing systems based on other transduction mechanisms (e.g., electro-chemical based sensors). If the PBG is located within the source wavelength range (for the case shown in Fig. 16, the upper edge of the PBG is used for the sensing), the PBG filters the optical source and the overlap of both spectra can be directly measured at the output using a simple power meter. When a variation of the refractive index of the surrounding medium occurs, it induces a shift in the spectral response of the photonic sensing structure. This is translated into a shift in the position of the PBG edge, and thus into a change in the optical power measured at the output, as is illustrated in Fig. 16 where an increase in the RI of the surrounding medium occurs. This power variation is directly used to perform the sensing, without the need to obtain the transmission spectrum of the structure using

expensive tunable elements. Moreover, since the output power can be continuously monitored (several power values per second can be measured), a real-time sensing is performed, which allows an instantaneous observation of the interactions taking place in the sensing structure.

The initial spectral alignment between the source and the sensor will determine the sensitivity and the linearity of the device. Eq. 1 describes the relative power variation at the output (in dB) as a function of the initial spectral overlap between source and sensor (BW) and the shift of the guided band's edge due to a change in the refractive index ($\Delta\lambda$).

$$10 \times \log_{10} \left(1 - \frac{\Delta\lambda}{BW} \right) \quad (1)$$

Fig. 17 shows the output power variation depending on the initial overlap between the source and the sensor. A high initial overlap leads to a linear response of the sensor, although a lower sensitivity is obtained. On the other hand, as the initial overlap is reduced, the sensitivity increases but a more non-linear behaviour is observed. However, a proper modeling and calibration of the sensor response will allow working in the non-linear regime, with a significant increase in the sensor sensitivity.

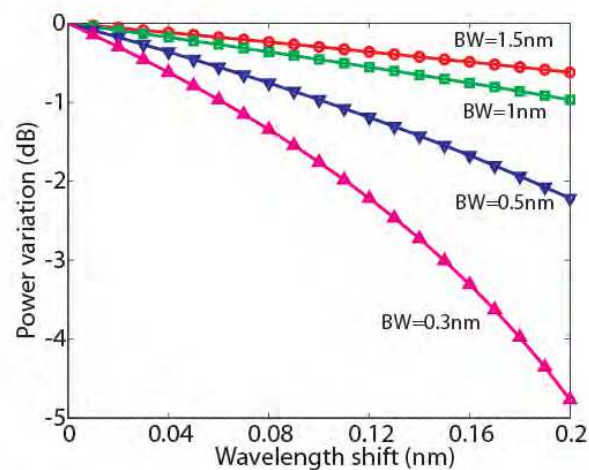


Fig. 17. Power variation versus wavelength shift for different initial alignments between the source and the sensor. BW indicates the initial overlapping bandwidth.

Another advantage of this readout technique is the possibility of continuously acquire the output power of the device (rigorously talking, many output power samples are taken each second). This will not only allow us to instantaneously observe any interaction taking place within the sensing device, but it will also allow to perform a temporal averaging of the power values and reduce the noise, thus leading to a significant reduction of the detection limit of the device.

7. Conclusion

Integrated planar photonic structures are one of the main candidates for the development of label-free biosensing devices, and among them, photonic crystal based structures. In this

chapter, we have shown how PCWs can be used for biosensing purposes and how the use of Fabry-Perot fringes appearing at the guided band's edge instead of the edge itself allows performing the sensing with a higher accuracy and leading to a reduced detection limit. Experimental results have been shown for the detection of refractive index variations (with a detection limit of 3.5×10^{-6} RIU), label-free antibody sensing (with a surface mass density detection limit below 2.1 pg/mm^2 and total mass detection limit below 0.2 fg), and label-free ssDNA sensing (with a detection limit of 19.8 nM).

A technique for the indirect tracking of the guided band's edge shift has also been presented. This technique avoids the use of expensive tunable sources or detectors, which are required when carrying out a direct tracking of the spectral response shift, as usually done when using photonic sensing devices such as ring resonators or photonic crystal based structures.

8. Acknowledgment

Financial support from the Spanish MICINN under contract TEC2008-06333, the Universidad Politécnic de Valencia through program PAID-06-09, and the Conselleria d'Educació through program GV-2010-031 is acknowledged.

9. References

- Barrios, C. A., Bañuls, M. J., González-Pedro, V., Gylfason, K. B., Sánchez, B., Griol, A., Maquieira, A., Sohlström, H., Holgado, M., & Casquel, R. (2008). Label-free optical biosensing with slot-waveguides. *Optics Letters*, Vol. 33, No. 7, (April 2008), pp. 708-710, ISSN 0146-9592
- Buswell, S. C., Wright, V. A., Buriak, J. M., Van, V., & Evoy, S. (2008). Specific detection of proteins using photonic crystal waveguides. *Optics Express*, Vol. 16, No. 20, (September 2008), pp. 15949-15957, ISSN 1094-4087
- Carlborg, C. F., Gylfason, K. B., Kaźmierczak, A., Dortu, F., Bañuls Polo, M. J., Maquieira Catala, A., Kresbach, G. M., Sohlström, H., Moh, T., Vivien, L., Popplewell, J., Ronan, G., Barrios, C. A., Stemme, G., & van der Wijngaart, W. (2010). A packaged optical slot-waveguide ring resonator sensor array for multiplex label-free assays in labs-on-chips. *Lab on a Chip*, Vol. 10, No. 3, (February 2010), pp. 281-290, ISSN 1473-0197
- Castelló, J.G., Toccafondo, V., Pérez-Millán, P., Losilla, N.S., Cruz, J.L., Andrés, M.V., & García-Rupérez, J. (2011). Real-time and low-cost sensing technique based on photonic bandgap structures *Optics Letters*, Vol. 36, No. 14, (July 2011), pp. 2707-2709, ISSN 0146-9592
- Chow, E., Grot, A., Mirkarimi, L. W., Sigalas, M., & Girolami, G. (2004). Ultracompact biochemical sensor built with two-dimensional photonic crystal microcavity. *Optics Letters*, Vol. 29, No. 10, (May 2004), pp. 1093-1095, ISSN 0146-9592
- De Vos, K., Bartolozzi, I., Schacht, E., Bienstman, P., & Baets, R. (2007). Silicon-on-Insulator microring resonator for sensitive and label-free biosensing. *Optics Express*, Vol. 15, No. 12, (June 2007), pp. 7610-7615, ISSN 1094-4087

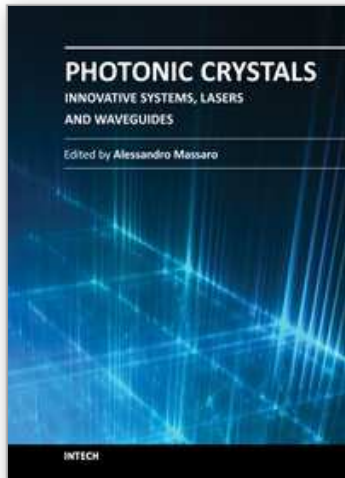
- De Vos, K., Girones, J., Popelka, S., Schacht, E., Baets, R., & Bienstman, P. (2009). SOI optical microring resonator with poly(ethylene glycol) polymer brush for label-free biosensor applications. *Biosensors and Bioelectronics*, Vol. 24, No. 8, (April 2009), pp. 2528-2533, ISSN 0956-5663
- Di Falco, A., O'Faolain, L., & Krauss, T. F. (2009). Chemical sensing in slotted photonic crystal heterostructure cavities. *Applied Physics Letters*, Vol. 94, No. 6, (February 2009), pp. 063503, ISSN 0003-6951
- Dorfner, D., Zabel, T., Hürlimann, T., Hauke, N., Frandsen, L., Rant, U., Abstreiter, G., & Finley, J. (2009). Photonic crystal nanostructures for optical biosensing applications. *Biosensors and Bioelectronics*, Vol. 24, No. 12, (August 2009), pp. 3688-3692, ISSN 0956-5663
- Fan, X. D., White, I. M., Shopova, S. I., Zhu, H., Suter, J. D., & Sun, Y. (2008). Sensitive optical biosensors for unlabeled targets: A review. *Analytica Chimica Acta*, Vol. 620, No. 1-2, (July 2008), pp. 8-26, ISSN 0003-2670
- García, J., Sanchis, P., & Martí, J. (2006). Detailed analysis of the influence of structure length on pulse propagation through finite-size photonic crystal waveguides. *Optics Express*, Vol. 14, No. 15, (July 2006), pp. 6879-6893, ISSN 1094-4087
- García, J., Sanchis, P., Martínez, A., & Martí, J. (2008). 1D periodic structures for slow-wave induced non-linearity enhancement. *Optics Express*, Vol. 16, No. 5, (March 2008), pp. 3146-3160, ISSN 1094-4087
- García-Rupérez, J., Toccafondo, V., Bañuls, M. J., Castelló, J. G., Griol, A., Peransi-Llopis, S., & Maquieira, Á. (2010). Label-free antibody detection using band edge fringes in SOI planar photonic crystal waveguides in the slow-light regime. *Optics Express*, Vol. 18, No. 23, (November 2010), pp. 24276-24286, ISSN 1094-4087
- Goddard, J.M., Mandal, S., Nugen, S.R., Baeumner, A.J., & Erickson, D. (2010). Biopatterning for label-free detection. *Colloids and Surfaces B: Biointerfaces*, Vol. 76, No. 1, (March 2010), pp. 375-380, ISSN 0927-7765
- Homola, J., Yee, S. S., & Gauglitz, G. (1999). Surface plasmon resonance sensors: review. *Sensors and Actuators, B: Chemical*, Vol. 54, No. 1, (January 1999), pp. 3-15, ISSN 0925-4005
- Huang, M., Yanik, A. A., Chang, T.-Y., & Altug, H. (2009). Sub-wavelength nanofluidics in photonic crystal sensors. *Optics Express*, Vol. 17, No. 26, (December 2009), pp. 24224-24233, ISSN 1094-4087
- Iqbal, M., Gleeson, M. A., Spaugh, B., Tybor, F., Gunn, W. G., Hochberg, M., Baehr-Jones, T., Bailey, R. C., & Gunn, L. C. (2010). Label-Free Biosensor Arrays Based on Silicon Ring Resonators and High-Speed Optical Scanning Instrumentation. *IEEE Journal on Selected Topics in Quantum Electronics*, Vol. 16, No. 3, (May 2010), pp. 654-661, ISSN 1077-260X
- Kauppinen, L. J., Hoekstra, H. J. W. M., & de Ridder, R. M. (2009). A compact refractometric sensor based on grated silicon photonic wires. *Sensors and Actuators, B: Chemical*, Vol. 139, No. 1, (May 2009), pp. 194-198, ISSN 0925-4005
- Kersey, A. D., Davis, M. A., Patrick, H. J., LeBlanc, M., Koo, K. P., Askins, C. G., Putnam, M. A., & Friebele E. J. (1997). Fiber Grating Sensors. *Journal of Lightwave Technology*, Vol. 15, No. 8, (August 1997), pp. 1442-1462, ISSN 0733-8724

- Lee, M. R., & Fauchet, P. M. (2007). Nanoscale microcavity sensor for single particle detection. *Optics Letters*, Vol. 32, No. 22, (November 2007), pp. 3284-3286, ISSN 0146-9592
- Loncar, M., Scherer, A., & Qiu, Y. (2003). Photonic crystal laser sources for chemical detection. *Applied Physics Letters*, Vol. 82, No. 26, (June 2003), pp. 4648-4650, ISSN 0003-6951
- Luff, B. J., Harris, R. D., Wilkinson, J. S., Wilson, R., & Schiffrin, D. J. (1996). Integrated-optical directional coupler biosensor. *Optics Letters*, Vol. 21, No. 8, (April 1996), pp. 618-620, ISSN 0146-9592
- Ramachandran, A., Wang, S., Clarke, J., Ja, S. J., Goad, D., Wald, L., Flood, E. M., Knobbe, E., Hryniewicz, J. V., Chu, S. T., Gill, D., Chen, W., King, O., & Little, B. E. (2008). A universal biosensing platform based on optical micro-ring resonators. *Biosensors and Bioelectronics*, Vol. 23, No. 7, (February 2008), pp. 939-944, ISSN 0956-5663
- Schubert, Th., Haase, N., Kück, H., & Gottfried-Gottfried, R. (1997). Refractive-index measurements using an integrated Mach-Zehnder interferometer. *Sensors and Actuators, A: Physical*, Vol. 60, No. 1-3, (May 1997), pp. 108-112, ISSN 0924-4247
- Scullion, M.G., Di Falco, A., & Krauss, T.F. (2011). Slotted Photonic Crystal Cavities with Integrated Microfluidics for Biosensing Applications. *Biosensors and Bioelectronics*, Vol. 27, No. 1, (September 2011), pp. 101-105, ISSN 0956-5663
- Sepúlveda, B., Río, J. S., Moreno, M., Blanco, F. J., Mayora, K., Domínguez, C., & Lechuga, L. M. (2006). Optical biosensor microsystems based on the integration of highly sensitive Mach-Zehnder interferometer devices. *Journal of Optics A: Pure and Applied Optics*, Vol. 8, No. 7, (July 2006), pp. S561-S566, ISSN 1464-4258
- Skivesen, N., Têtu, A., Kristensen, M., Kjems, J., Frandsen, L. H., & Borel, P. I. (2007). Photonic-crystal waveguide biosensor. *Optics Express*, Vol. 15, No. 6, (March 2007), pp. 3169-3176, ISSN 1094-4087
- Sünner, T., Stichel, T., Kwon, S.-H., Schlereth, T. W., Höfling, S., Kamp, M., & Forchel, A. (2008). Photonic crystal cavity based gas sensor. *Applied Physics Letters*, Vol. 92, No. 26, (July 2008), pp. 261112, ISSN 0003-6951
- Toccafondo, V., García-Rupérez, J., Bañuls, M. J., Griol, A., Castelló, J. G., Peransi-Llopis, S., & Maquieira, A. (2010). Single-strand DNA detection using a planar photonic-crystal-waveguide-based sensor. *Optics Letters*, Vol. 35, No. 21, (November 2010), pp. 3673-3675, ISSN 0146-9592
- Xu, D.-X., Vachon, M., Densmore, A., Ma, R., Delâge, A., Janz, S., Lapointe, J., Li, Y., Lopinski, G., Zhang, D., Liu, Q. Y., Cheben, P., & Schmid, J. H. (2010). Label-free biosensor array based on silicon-on-insulator ring resonators addressed using a WDM approach. *Optics Letters*, Vol. 35, No. 16, (August 2010), pp. 2771-2773, ISSN 0146-9592
- Xu, T., Zhu, N., Xu, M. Y.-C., Wosinski, L., Aitchison, J. S., & Ruda, H. E. (2010). Pillar-array based optical sensor. *Optics Express*, Vol. 18, No. 6, (March 2010), pp. 5420-5425, ISSN 1094-4087

Zlatanovic, S., Mirkarimi, L. W., Sigalas, M. M., Bynum, M. A., Chow, E., Robotti, K. M., Burr, G. W., Esener, S., & Grot, A. (2009). Photonic crystal microcavity sensor for ultracompact monitoring of reaction kinetics and protein concentration. *Sensors and Actuators, B: Chemical*, Vol. 141, No. 1, (August 2009), pp. 13-19, ISSN 0925-4005

IntechOpen

IntechOpen



Photonic Crystals - Innovative Systems, Lasers and Waveguides

Edited by Dr. Alessandro Massaro

ISBN 978-953-51-0416-2

Hard cover, 348 pages

Publisher InTech

Published online 30, March, 2012

Published in print edition March, 2012

The second volume of the book concerns the characterization approach of photonic crystals, photonic crystal lasers, photonic crystal waveguides and plasmonics including the introduction of innovative systems and materials. Photonic crystal materials promises to enable all-optical computer circuits and could also be used to make ultra low-power light sources. Researchers have studied lasers from microscopic cavities in photonic crystals that act as reflectors to intensify the collisions between photons and atoms that lead to lasing, but these lasers have been optically-pumped, meaning they are driven by other lasers. Moreover, the physical principles behind the phenomenon of slow light in photonic crystal waveguides, as well as their practical limitations, are discussed. This includes the nature of slow light propagation, its bandwidth limitation, coupling of modes and particular kind terminating photonic crystals with metal surfaces allowing to propagate in surface plasmon-polariton waves. The goal of the second volume is to provide an overview about the listed issues.

How to reference

In order to correctly reference this scholarly work, feel free to copy and paste the following:

Jaime García-Rupérez, Veronica Toccafondo and Javier García Castelló (2012). Label-Free Biosensing Using Photonic Crystal Waveguides, Photonic Crystals - Innovative Systems, Lasers and Waveguides, Dr. Alessandro Massaro (Ed.), ISBN: 978-953-51-0416-2, InTech, Available from:
<http://www.intechopen.com/books/photonic-crystals-innovative-systems-lasers-and-waveguides/label-free-biosensing-using-photonic-crystal-waveguides>

INTECH
open science | open minds

InTech Europe

University Campus STeP Ri
Slavka Krautzeka 83/A
51000 Rijeka, Croatia
Phone: +385 (51) 770 447
Fax: +385 (51) 686 166
www.intechopen.com

InTech China

Unit 405, Office Block, Hotel Equatorial Shanghai
No.65, Yan An Road (West), Shanghai, 200040, China
中国上海市延安西路65号上海国际贵都大饭店办公楼405单元
Phone: +86-21-62489820
Fax: +86-21-62489821

© 2012 The Author(s). Licensee IntechOpen. This is an open access article distributed under the terms of the [Creative Commons Attribution 3.0 License](#), which permits unrestricted use, distribution, and reproduction in any medium, provided the original work is properly cited.

IntechOpen

IntechOpen